Supplementary Information: Structured environments fundamentally alter dynamics and stability of ecological communities

Nick Vallespir Lowery and Tristan Ursell
Department of Physics, University of Oregon
Eugene, Oregon USA

1 Calculating Maximum Interface Curvature in a Pillar Lattice

We assume that all competition interfaces between pillars make right angles with the pillar edges. We also center the system such that we eliminate a parameter and then the equation of the circle that approximates the competition interface is

$$x^2 + (y - y_o)^2 = r^2, \tag{1}$$

where r is the radius of the circle whose edge is the competition interface and y_o is the y coordinate of that circle. We assume that the center-to-center separation of the pillars is Δx and the radius of each pillar is R. We characterize the point of intersection between the pillar edge and the circular interface by the angle ϕ. Then at the point of intersection (i) between the circle and the pillar the coordinates on the circle are

$$x_i = -\frac{\Delta x}{2} + R\cos(\phi) \;\text{ and }\; y_i = R\sin(\phi). \tag{2}$$

At that same point the slope of the circle must be equal to $\tan(\phi)$. The slope is found by taking the implicit derivative

$$\frac{\partial}{\partial x}\left[x^2 + (y - y_o)^2 = r^2\right] \;\rightarrow\; 2x + 2(y - y_o)y_x = 0 \;\rightarrow\; y_x = -\frac{x}{y - y_o}, \tag{3}$$

and using this result we can solve for y_o and use that to find r^2

$$\left(\frac{r}{R}\right)^2 = \left(\frac{\delta - \cos(\phi)}{\sin(\phi)}\right)^2 \;\rightarrow\; \frac{r}{R} = \frac{\delta - \cos(\phi)}{\sin(\phi)} \tag{4}$$

where the sign ambiguity is irrelevant, and we define $\delta = \frac{\Delta x}{2R}$. Then the minimum radius (maximum curvature) lies at the angle given by

$$\frac{\partial}{\partial \phi}\left(\frac{r}{R}\right) = 0 \;\rightarrow\; \phi_c = \tan^{-1}\left(\sqrt{1 - \frac{1}{\delta^2}}, \frac{1}{\delta}\right), \tag{5}$$

where we use the four-quadrant tangent function, and upon substitution

$$\frac{r_{\min}}{R} = \sqrt{\delta^2 - 1}, \tag{6}$$

and thus the maximum curvature is

$$\kappa_{\max} = \frac{1}{R\sqrt{\delta^2 - 1}}. \tag{7}$$

We note that as $\delta \rightarrow \infty$ the maximum curvature goes to zero and the circle that corresponds to the maximum curvature is the circle whose diameter is Δx. As $\delta \rightarrow 1$ (and hence $\Delta x \rightarrow 2R$) the maximum curvature diverges.

www.pnas.org/cgi/doi/10.1073/pnas.1811887115

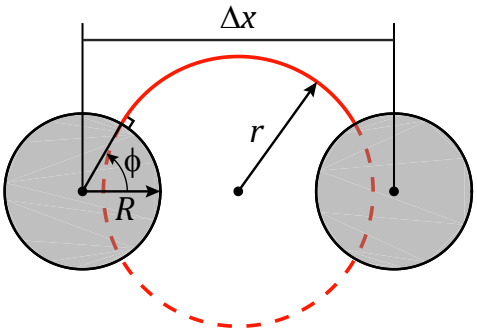

SI Figure 1: Schematic graphically depicting the pillar radius R, pillar separation Δx, and angle ϕ. For fixed values of R and Δx, each interface curvature $1/r$ corresponds to a contact angle ϕ.

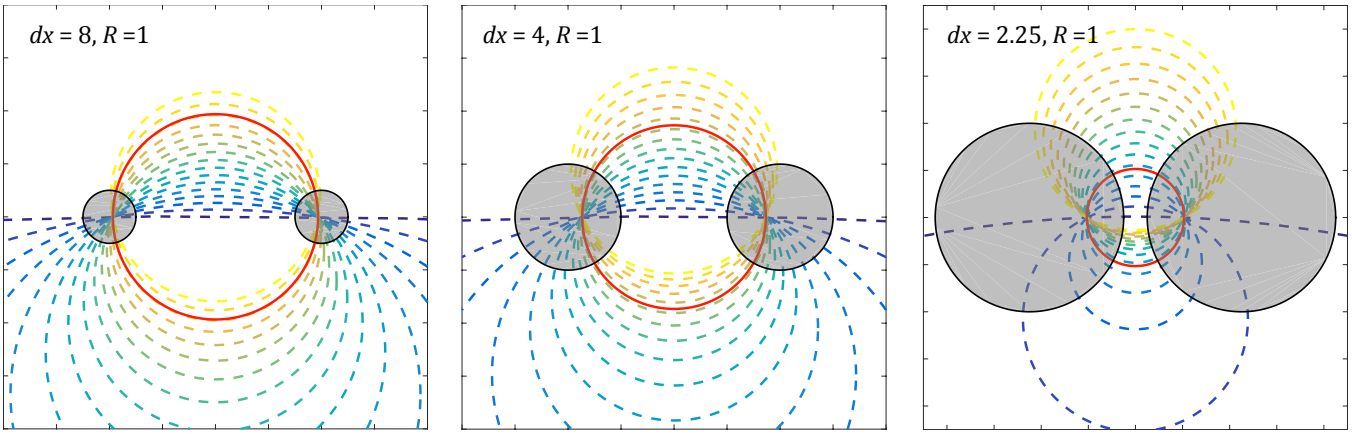

SI Figure 2: Plots of maximum interface curvature as a function of pillar separation. The dashed lines show the interface curvature as a function of the angle ϕ, from low ϕ (blue) to high ϕ (yellow). The solid red circle shows the circle whose corresponding competitive interface has the highest curvature given the values of R and Δx.

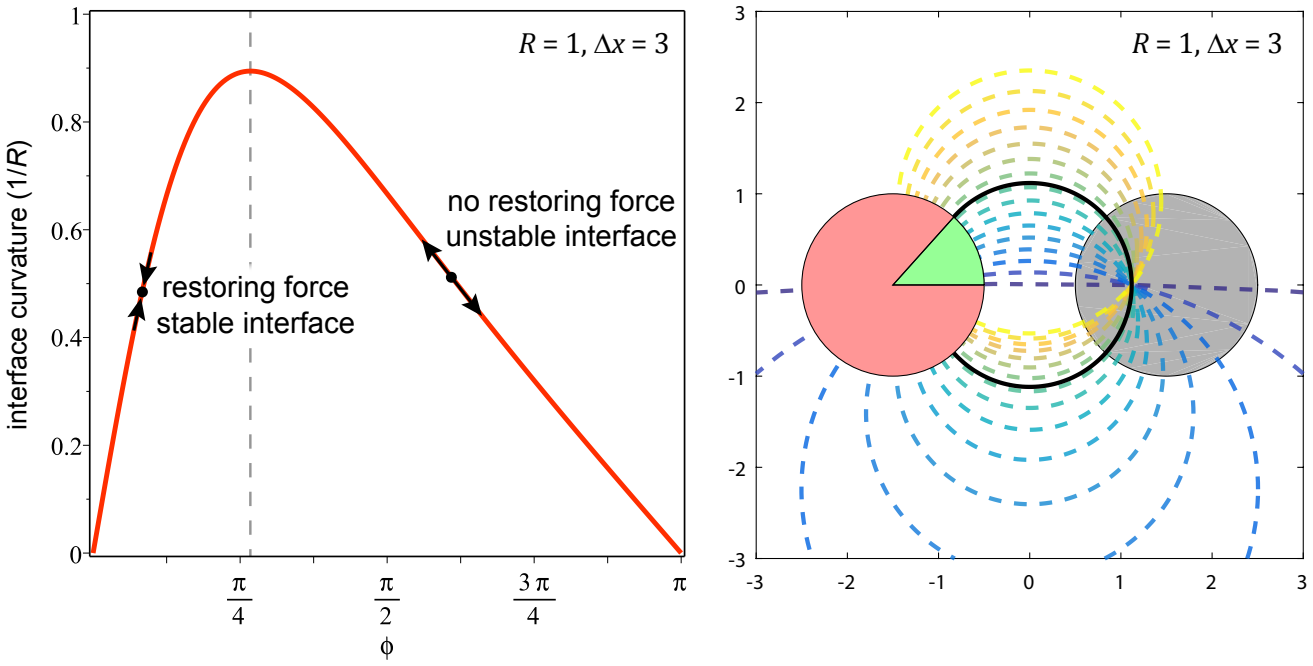

SI Figure 3: (A) Plot of the interface curvature between two pillars with the indicated size and spacing as a function of the contact angle ϕ. If the ecologically equilibrated interface curvature is both less than the maximum curvature and corresponds to a contact angle less than the contact angle at maximum curvature then the dynamics provide a restoring force which stabilizes the interface, otherwise, the interface is unstable. (B) Schematic matched to (A) that shows the zone of stable interface angles ϕ in green (here $0 \leq \phi_{\text{stable}} \lesssim \pi/4$) and unstable zone in red. The maximum angle of the green zone and the black circle both correspond to the maximum curvature shown in (A).

1.1 Relationship to Competitive Asymmetry

We can calculate the maximum possible curvature for a particular lattice with values R and Δx, and if a particular level of competitive asymmetry, $\epsilon = \frac{1}{2}|P_{AB} - P_{BA}|$, between species A and B requires a higher curvature than this value, the lattice in question will not stably support both species.

We know that competition interfaces are flat for symmetric competition ($\epsilon = 0$), while $\epsilon > 0$ results in curved interfaces. Additionally, the sharpness of the competitive interface is inversely related to $\langle P \rangle = \frac{1}{2}(P_{AB} + P_{BA})$; the lower the mean value of P the sharper the interface. Thus dimensional arguments demand that the curvature of the competitive interface be set by a function of the dimensionless competition asymmetry, $\epsilon / \langle P \rangle$. The inverse natural length scale of the system $\frac{1}{\lambda} = \sqrt{r/D}$, sets the natural scale for curvature and thus to within a constant the interface curvature in a stable competitive system must be

$$\kappa_{\text{crit}} = \sqrt{\frac{r}{D}} f\left(\frac{\epsilon}{\langle P \rangle}\right). \tag{8}$$

where f is some function. Taylor's theorem then suggests that for a sufficiently smooth function with small dimensionless competitive asymmetries

$$\kappa_{\text{crit}} \propto \sqrt{\frac{r}{D}} \frac{\epsilon}{\langle P \rangle} \tag{9}$$

which is supported by the data in Fig. 2B.

A geometric argument gives similar results; given two strains with unequal competitive fitness, we postulate that at equilibrium (i.e. when the genetic boundary does not move) the ratio of competition parameters P_{AB} and P_{BA} is proportional to the ratio of the numeric advantage imposed by a curved interface (as shown in SI Fig. 4). The width of the transition zone, w, is, to within an order one constant, set by the only natural length scale in the system, $\sqrt{D/r}$, and hence this implies

$$\frac{P_{AB}}{P_{BA}} \propto \frac{\pi(R^2 - (R - \frac{w}{2})^2)}{\pi((R + \frac{w}{2})^2 - R^2)} \text{ with } \kappa_{\text{crit}} = \frac{1}{R} \rightarrow \kappa_{\text{crit}} \propto \frac{1}{w} \frac{P_{AB} - P_{BA}}{P_{AB} + P_{BA}} \propto \sqrt{\frac{r}{D}} \frac{\epsilon}{\langle P \rangle}. \tag{10}$$

2 Demonstration of Positive Lyapunov Exponents

In the main text we employed correlation analysis to examine the three-component dynamical state, outside of stable limit-cycling, showing extreme sensitivity to initial conditions as a rapid decay in the correlation between nearly identical initial conditions. Here, we examine how the abundance of three intransitively competing species evolve from a conserved initial state with a small perturbation. We simulated the three component system with a random initial condition for 200 doubling times to create a state whose spatial structure was well past the 'grow in' period – we refer to this as the 'seed' state. We then generated zero-mean Gaussian noise with a standard deviation of 0.001 in units of carrying capacity and added unique instances of this noise to 30 independent replicates of the seed state. We evolved each of those replicates for an additional 600 doubling periods. For each replicate, we calculated the absolute difference in concentration at every position between the time-matched evolved seed state and each of the 30 perturbed states. We calculated the natural logarithm of each of these state-distance vectors through time and averaged them, giving the log-mean magnitude of the state-distance as a function of time. Because each component A_i is bounded by $0 \leq A_i \leq 1$ the state-distances are bounded, but for early times the slope of the log-mean magnitude approximates the maximal Lyapunov exponent [1]. As shown in SI Fig. 5 small perturbations from the seed state: (i) led to exponentially increasing state-distances, indicating positive Lyapunov exponents, (ii) showed clear and rapidly increasing divergences in component abundances through time from a nearly identical state, commensurate with (i), and (iii) evolved spatial patterns that were initially similar but ultimately significantly diverged over time.

Following the same protocol as above, we performed demonstrative simulations of three-species dynamics in a typical Lotka-Volterra model with dense pillars and calculated the state distance vectors for 30

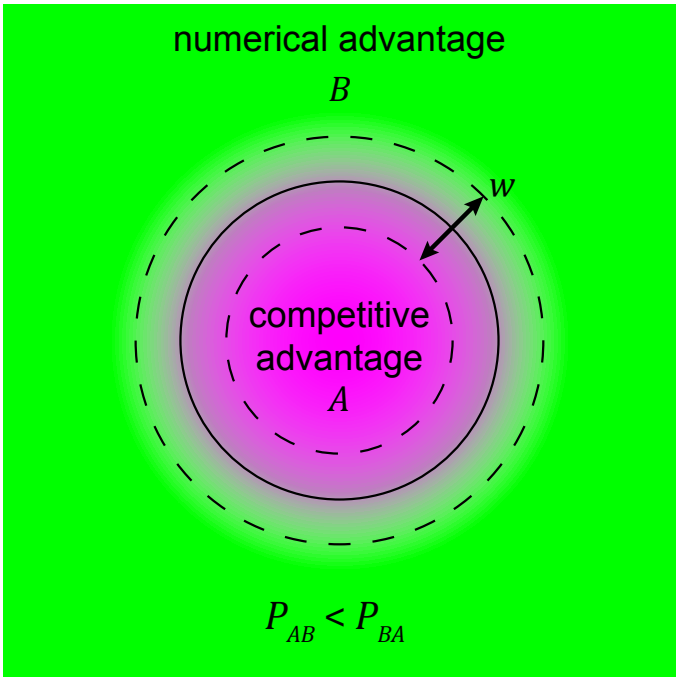

SI Figure 4: A schematic of the unstable equilibrium between two unequal competitors, here with species A (magenta) the stronger competitor (hence $P_{AB} < P_{BA}$). The competition zone has a width w set by the natural length scale $\sqrt{D/r}$. The equilibrium curvature of the competitive interface (solid line) is positioned such that the numerical advantage of the weaker competitor (B) is balanced against the higher potency of the stronger competitor (A). In the absence of structural perturbations (e.g. pillars) this equilibrium is unstable.

replicates over a period of 400 doubling times. Like the modified LV model, introduction of dense pillars led to extreme sensitivity to perturbation and chaotic dynamics, while the absence of pillars was insensitive to perturbations and did not display chaotic dynamics (see SI Fig.6). When pillars were present, the state distance increased approximately exponentially at early times indicating a positive maximal Lyapunov exponent. While we did not run an exhaustive set of simulations for the typical LV model, we noticed that denser pillar arrays were required to elicit chaotic dynamics as compared to the modified LV model.

Caption for SI Figure 5: Demonstration of Chaotic Dynamics. This figure expands on the data from Fig. 3, with each labeled row in this figure corresponding to a column in Fig. 3. From an initially random state we simulated our modified Lotka-Volterra equations for 200 doubling times to establish an initial 'seed' state. At $t = 200$ (dashed vertical lines in the first column) we created 30 identical replicates of the seed state and to each added unique instances of zero-mean Gaussian noise with a standard deviation of 0.001. The first column shows the subsequent evolution of the mean abundance of all 30 perturbed replicates to the right of the dashed vertical line. The second column shows the natural log of the state distance from the original seed starting at $t = 200$. The third column shows the seed state at the time of perturbation (upper left) followed by three perturbed replicates. The first row corresponds to Fig. 3A and shows little sensitivity to perturbations, sublinear growth of the state distance with time, and the terminal states for each replicate are nearly identical, with per-pixel differences in abundance at $\sim 10^{-4}$. The second row corresponds to Fig. 3B, there is some sensitivity to perturbations, but the state distance grows slower than exponentially with time and hence is not chaotic, accordingly the three replicates are also nearly identical, with per-pixel differences in abundance at $\sim 10^{-2}$. The third row corresponds to Fig. 3C; at this reduced pillar spacing the replicates show extreme sensitivity to perturbations and the state distance grows exponentially with time up to a saturation level imposed by the bounds of A_i, and accordingly, the replicates are distinctly different a fixed time after perturbation. The fourth row corresponds to Fig. 3D and like the previous row, at this pillar spacing there is extreme sensitivity to perturbations, exponential growth of state distances, and the species distributions for each replicate are distinct. In the third and fourth rows, the slope of the log-linear (exponential) increase in state distances approximates the maximal Lyapunov exponent, which is positive, indicating chaotic dynamics. In all simulations, $L/(1.29\lambda) = 150$, $D = 15$, $P = 0.1$, and $A_{\min} = 0$, R, and Δx as indicated in Fig. 3.

Caption for SI Figure 6: Perturbations to a typical Lotka-Volterra model. From an initially random state we simulated a typical Lotka-Volterra model (first through third rows) to establish an initial 'seed' state. We created 30 identical replicates of the seed state and to each added unique instances of zero-mean Gaussian noise with a standard deviation of 0.001. The first column shows the subsequent evolution of the mean abundance of all 30 perturbed replicates to the right of the dashed vertical line. The second column shows the natural log of the state distances from the seed state. The third column shows the seed state (upper left) followed by three perturbed replicates. The first row is a typical LV model without pillars and shows little sensitivity to perturbations, essentially no growth of state distance with time, and nearly identical replicates, with per-pixel differences in abundance at $\sim 10^{-4}$. The second row is a typical LB model perturbed by pillars spaced at $\Delta x = 5.5R$ and shows little sensitivity to perturbations, essentially no growth of state distance with time, and nearly identical replicates, with per-pixel differences in abundance at $\sim 10^{-4}$. The third row is a typical LV model with pillars at a denser spacing of $\Delta x = 4R$, showing extreme sensitivity to perturbations and approximately exponential growth of state distance with time, indicating chaotic dynamics. Accordingly the three replicates are each distinct. The third row is the modified LV model with the same pillar conditions as the second row for comparison. Like the data from Fig. 3D, this row shows extreme sensitivity to perturbations and the state distance grows exponentially with time up to a saturation level imposed by the bounds of A_i, and accordingly, the replicates are distinctly different a fixed time after perturbation. In the second and third rows, the slope of the log-linear (exponential) increase in state distances approximates the maximal Lyapunov exponent, which is positive, indicating chaotic dynamics. In all simulations, $L/(1.29\lambda) = 150$, $D = 15$, $P = 0.1$, and $A_{\min} = 0$, and R and Δx as

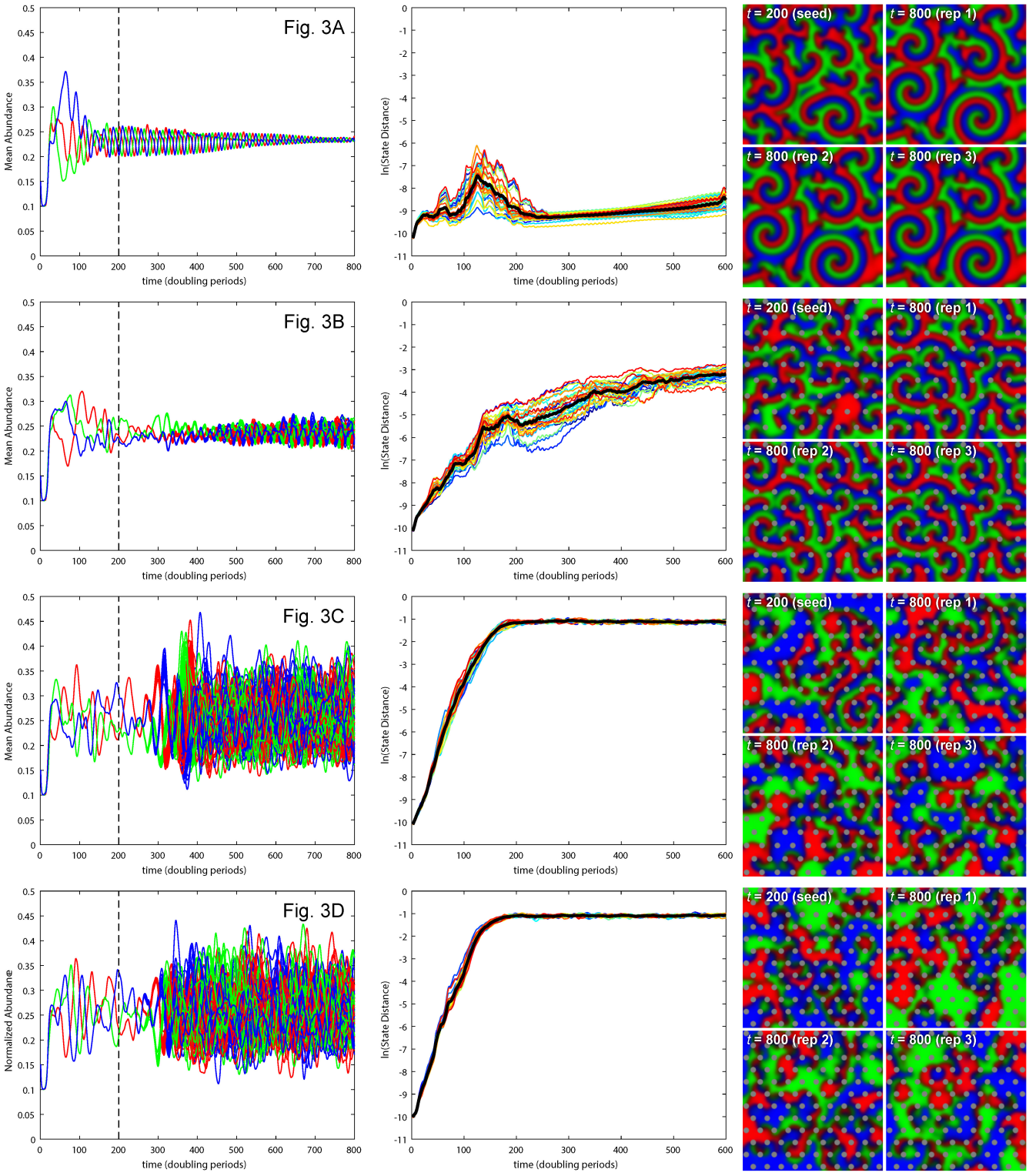
Fig. 3A
Fig. 3B
Fig. 3C
Fig. 3D
Mean Abundance
Normalized Abundance
ln(State Distance)
time (doubling periods)
t = 200 (seed)
t = 800 (rep 1)
t = 800 (rep 2)
t = 800 (rep 3)

SI Figure 5:

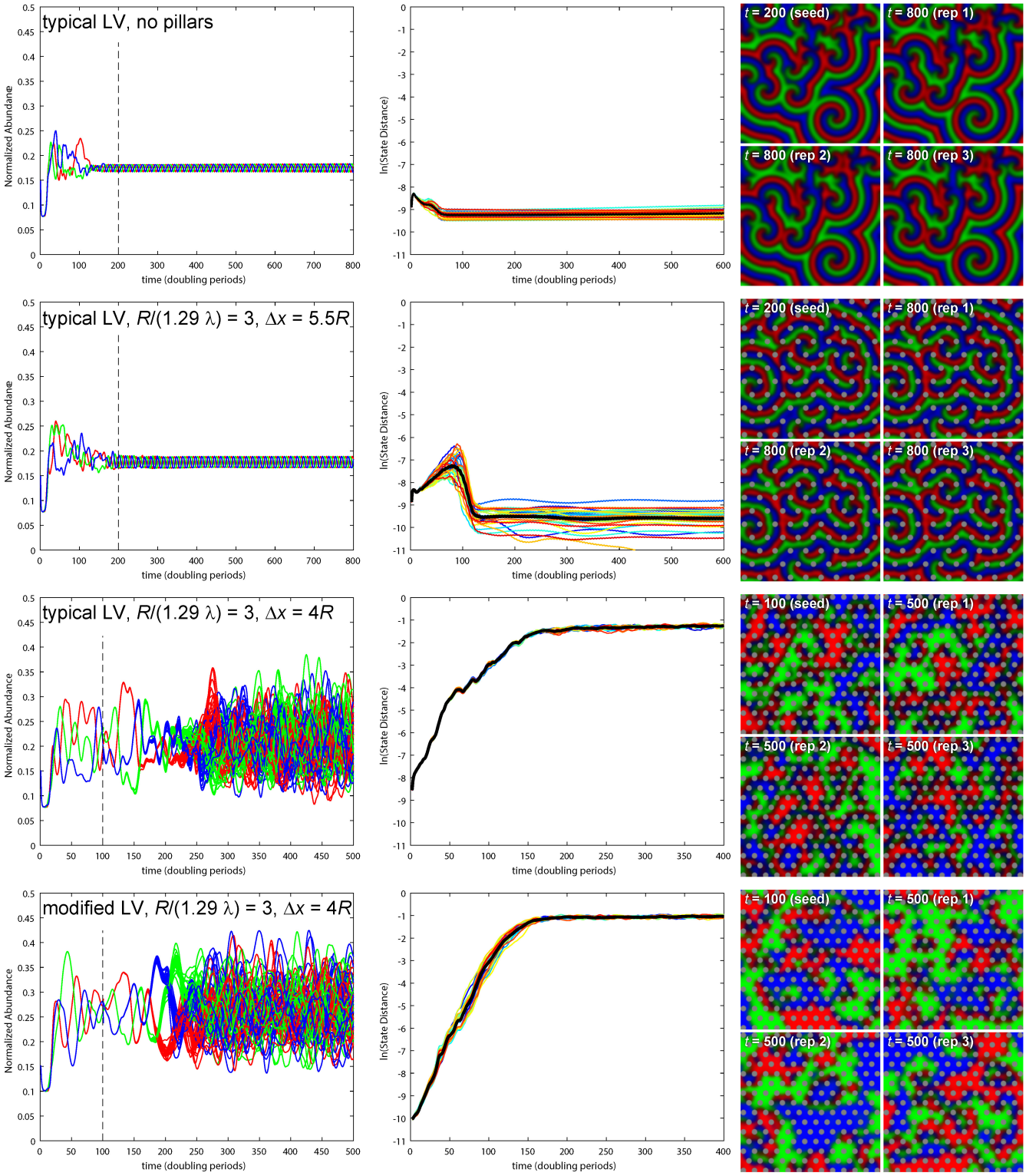
typical LV, no pillars
typical LV, R/(1.29 λ) = 3, Δx = 5.5R
typical LV, R/(1.29 λ) = 3, Δx = 4R
modified LV, R/(1.29 λ) = 3, Δx = 4R
Normalized Abundance
ln(State Distance)
time (doubling periods)
t = 200 (seed)
t = 800 (rep 1)
t = 800 (rep 2)
t = 800 (rep 3)
t = 100 (seed)
t = 500 (rep 1)
t = 500 (rep 2)
t = 500 (rep 3)

SI Figure 6:

indicated.

3 Relationship to Typical Lotka-Volterra Model

For both the two and three component systems, our model equations are symmetric between components and are represented in dimensionless form by

$$\frac{\partial A_i}{\partial t} = \nabla^2 A_i + A_i \left(1 - \frac{A_k}{P_{ki}}\right) \left(1 - \sum_j A_j\right), \tag{11}$$

where A_k actively kills A_i and the sum over j includes all species. For simplicity, this model does not explore differences in carrying capacity. We note that if the concentration, P_{ki}, of an opposing species, A_k, that is required to induce local killing in A_i is very large relative to the carrying capacity C, (that is $P_{ki}/C \gg 1$) then this model becomes a typical Lotka-Volterra model with identical carrying capacity between the species, given by

$$\frac{\partial A_i}{\partial t} = \nabla^2 A_i + A_i \left(1 - \sum_j A_j\right). \tag{12}$$

For finite values of P_{ki}, the difference between our model and a typical Lotka-Volterra model is the inclusion of cubic terms of the form A^2B, AB^2, and ABC for the three component case, and A^2B and AB^2 for the two component case. In most regions of space where one species dominates, these terms are guaranteed to be small, because at most an $O(1)$ component is being multiplied by one or two powers of a component that is $\ll 1$. The inclusion of the term $1 - A_k/P_{ki}$ is meant to capture active killing at the interface between two species by parameterizing species-specific interactions that are independent of resource limitations, i.e. active killing, and as such these cubic terms are most significant at interfaces. In SI Fig. 7 we compare structurally induced coexistence between mutual killers in both a typical and our modified Lotka-Volterra equations; we reduced our modified model to a typical Lotka-Volterra type via the transformation

$$\frac{\partial A_i}{\partial t} = \nabla^2 A_i + A_i \left(1 - \frac{A_k}{P_{ki}}\right) \left(1 - \sum_j A_j\right) \quad \rightarrow \quad \frac{\partial A_i}{\partial t} = \nabla^2 A_i + A_i \left(1 - \sum_j A_j - \frac{A_k}{P_{ki}}\right), \tag{13}$$

by removing cubic terms. Further, we used this typical form to recalculate the extinction probability phase plot of Fig. 2A from the main text, shown below in SI Fig. 8.

4 Modeling Extinction Time Distributions in Structured Environments

We seek to characterize the classes of dynamics observed during three-way intransitive competition in our anisotropic environmental simulations. The diagram below shows the states and transition rates between the three observed dynamical states, with L being limit-cycle (cyclic), C being chaotic, and E being extinction. Extinction is a fully absorbing state (hence no arrows emerge from E). The cyclic state is characterized by stable coexistence of all three species and hence the transition rate from L to E is strictly modeled as zero. Our simulations are deterministic and hence for a given initial condition in a particular environment the time course of transitions between these states is encoded by those initial conditions. Thus the ensemble from which we draw trajectories that statistically follow this diagram is the ensemble of random, spatially uncorrelated initial conditions, not a statistical ensemble over stochastic dynamical processes.

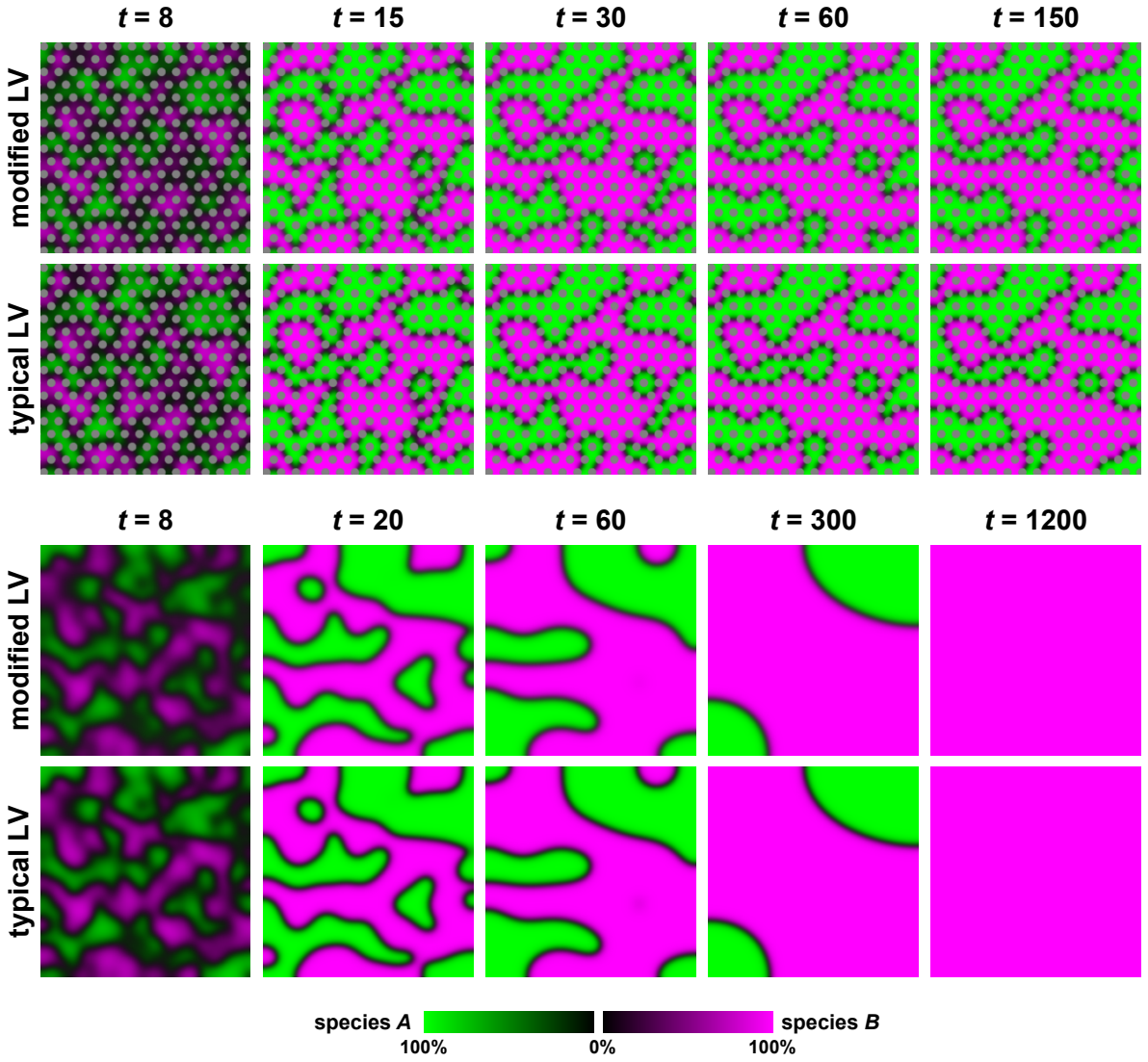

SI Figure 7: Comparison of our modified Lotka-Volterra model to a typical Lotka-Volterra model with two species. The top two rows show the evolution of both models in identical structured grids with identical initial conditions. Their subsequent evolution is very similar and ultimately a stable pattern of coexistence is established. Grid parameters were $R/(1.29\lambda) = 2$ and $\Delta x = 3.5R$. The bottom two rows show the evolution of both models with identical initial conditions in the absence of any environmental structure. Their subsequent evolution is very similar and ultimately both models coarsen until there is single dominant species. In all simulations, $L/(1.29\lambda) = 100$, $D = 15$, $P = 0.1$, and $A_{\min} = 0.001$.

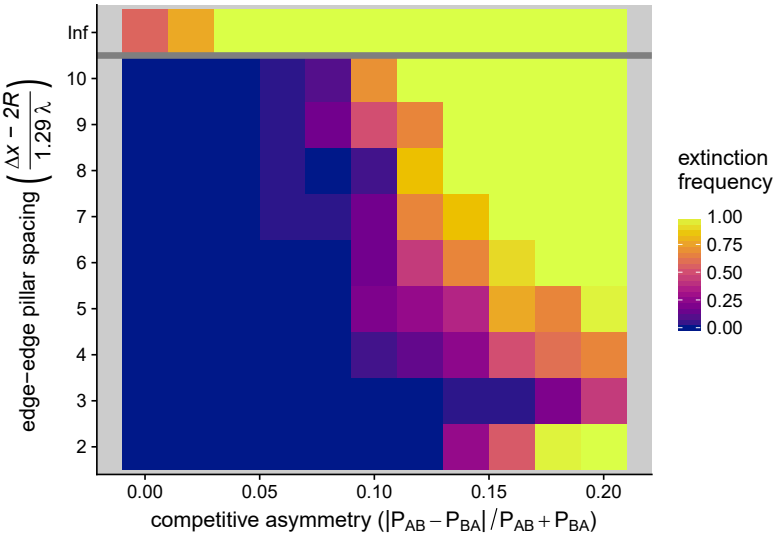

SI Figure 8: Reproduction of Fig. 2A using the standard Lotka-Volterra model, showing nearly identical behavior of coexistence between mutual killers that depends on pillar-grid parameters. In all simulations, $L/(1.29\lambda) = 100$, $D = 15$, $\langle P \rangle = 0.1$, and $A_{\min} = 0.001$.

4.1 Kinetic Model

We assume that for a given pillar size and spacing, there is a corresponding set of state-transition rates. Over an ensemble of initial conditions, these rates are characterized by the number of observed transitions of a particular type (CL, LC, or CE) per unit time. This model aims to determine the distribution of arrival times into the extinct state and compare those predictions with the simulated distributions. The distribution of arrival times $p(t')$ is related to the extinct ensemble fraction E by

$$dE = p(t')dt' \quad \rightarrow \quad p(t') = \frac{\partial E}{\partial t'} \tag{14}$$

where the total integrated amount of E is 1 as $t' \to \infty$ because E is a strictly absorbing state. This means that all trajectories eventually end with extinction, though the time to extinction could be very long if, for instance, specific values of pillar size and spacing result in $k_{LC} \sim 0$, noting that as $\Delta x \to \infty$, $k_{LC} \to 0$.

Using this kinetic model, the following ODEs govern the probability of being in each state as a function of time

$$\dot{L} = -k_{LC}L + k_{CL}C \tag{15}$$

$$\dot{C} = k_{LC}L - (k_{CL} + k_{CE})C \tag{16}$$

$$\dot{E} = k_{CE}C \tag{17}$$

Since this describes the time-dependent probability of being in a given state $\dot{L} + \dot{C} + \dot{E} = 0$ and hence the system is conservative. Given that $\dot{E} \propto C$, we note that $C \propto p(t)$ and hence seek to decouple the equations into an equation strictly for C. Solving eqn. 16 for L we find

$$L = \frac{1}{k_{LC}}\left(\dot{C} + (k_{CL} + k_{CE})C\right) \tag{18}$$

and then differentiating with respect to time we find

$$\dot{L} = \frac{1}{k_{LC}}\left(\ddot{C} + (k_{CL} + k_{CE})\dot{C}\right). \tag{19}$$

Then substituting these into eqn. 15 we have

$$\dot{L} = -k_{LC}L + k_{CL}C \quad \rightarrow \quad \frac{1}{k_{LC}}\left(\ddot{C} + (k_{CL}+k_{CE})\dot{C}\right) = -k_{LC}\frac{1}{k_{LC}}\left(\dot{C} + (k_{CL}+k_{CE})C\right) + k_{CL}C \tag{20}$$

which simplifies to

$$\ddot{C} + (k_{LC}+k_{CL}+k_{CE})\dot{C} + k_{LC}k_{CE}C = 0. \tag{21}$$

We note that the two initial conditions that connect to our simulations are $C(0) = C_o$ and $L(0) = L_o$, which then translate into $C(0) = C_o$ and

$$\dot{C}(0) = k_{LC}L_o - (k_{CL}+k_{CE})C_o. \tag{22}$$

In order to reduce the parameter space and reveal natural scales, we non-dimensionalize this equation by choosing a time scale that is positive and bounded as individual rate constants are set to zero, $k_{ij} \to 0$, namely

$$t' = t\tau \quad \rightarrow \quad \tau = (k_{LC}+k_{CL}+k_{CE})^{-1}. \tag{23}$$

Then switching to the dimensionless t as the time variable, we have

$$\ddot{C} + \dot{C} + KC = 0 \tag{24}$$

with the dimensionless constant

$$K = \frac{k_{LC}k_{CE}}{(k_{LC}+k_{CL}+k_{CE})^2}. \tag{25}$$

The rate constants are all positive, $k_{ij} \geq 0$, and hence it can be shown that

$$0 < K < \frac{1}{4} \tag{26}$$

for all values of k_{ij}[1]. This also transforms the initial condition to

$$\dot{C}(0) = \tau\left(k_{LC}L_o - (k_{CL}+k_{CE})C_o\right) = \tau k_{LC}L_o + (\tau k_{LC} - 1)C_o. \tag{27}$$

4.1.1 Initial Condition $C(0) = 0$ $L(0) = 1$

There are two solutions of interest, namely when $(C_o, L_o) = (0, 1)$ and $(C_o, L_o) = (1, 0)$. Any other initial condition is a linear combination of these two solutions. Let us examine $(C_o, L_o) = (0, 1)$, which has the solution

$$C(t) = \tau k_{LC}\frac{e^{-\frac{t}{2}}}{\alpha}\sinh(\alpha t) \tag{28}$$

with $\alpha = \frac{\sqrt{1-4K}}{2}$. Then building on the fact that $\dot{E} = k_{CE}C = p(t)$

$$p_{01}(t) = \dot{E} = \tau k_{CE}C(t) = \frac{K}{\alpha}e^{-\frac{t}{2}}\sinh(\alpha t) \tag{29}$$

where the factor of τ comes from the non-dimensionalization and the subscript 01 in p refers to the initial conditions used to derive this version of p. On long time scales

$$\int_0^\infty p_{01}(t)\mathrm{d}t = \frac{K}{\alpha}\int_0^\infty e^{-\frac{t}{2}}\sinh(\alpha t)\,\mathrm{d}t = \frac{\frac{1}{4}-\alpha^2}{\alpha}\int_0^\infty e^{-\frac{t}{2}}\sinh(\alpha t)\,\mathrm{d}t = 1 \tag{30}$$

for all values of $0 < \alpha < \frac{1}{2}$, meaning all trajectories lead to the fully absorbing state of extinction.

[1] Examining $K' = \frac{ab}{(a+b)^2}$, which is maximized when $a = b$ and hence $K' = \frac{1}{4}$. Then changing to $K'' = \frac{ab}{(a+b+c)^2}$ with $c > 0$ and hence $0 < K'' \leq K'$.

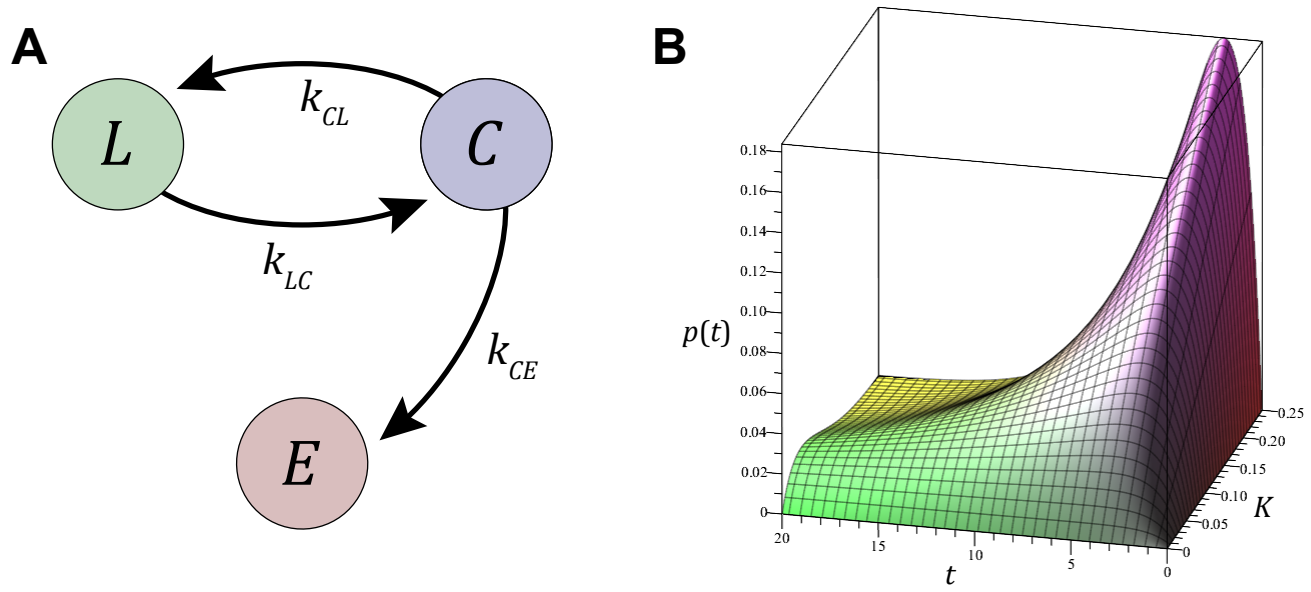

SI Figure 9: (A) Schematic showing dynamical states (limit-cycle / cyclic L, chaotic C, and extinct E) and the mean rates of transition that connect them. (B) The family of extinction time distributions as a function of dimensionless time and the dimensionless rate parameter K for $C(0) = 0$ and $L(0) = 1$ that result from the kinetic model in (A).

4.1.2 Initial Condition $C(0) = 1$ $L(0) = 0$

Examining $(C_o, L_o) = (1, 0)$, combining terms and simplifying, this has the solution

$$C(t) = \frac{e^{-\frac{t}{2}}}{2\alpha} \left[2\alpha \cosh(\alpha t) + (2\tau k_{LC} - 1) \sinh(\alpha t)\right] \tag{31}$$

and then $p_{10}(t) = \dot{E} = \tau k_{CE} C(t)$ and hence

$$p_{10}(t) = \frac{K}{\alpha} e^{-\frac{t}{2}} \sinh(\alpha t) + \gamma \frac{e^{-\frac{t}{2}}}{2\alpha} \left[2\alpha \cosh(\alpha t) - \sinh(\alpha t)\right] \tag{32}$$

with

$$\int_0^\infty p_{10}(t) \mathrm{d}t = 1. \tag{33}$$

The dimensionless constant $\gamma = \tau k_{CE}$ is bounded to be $0 < \gamma < 1$. We note that the first term in the above equation is the solution for $p_{01}(t)$ that we found for $C(0) = 0$ and $L(0) = 1$, that solution integrates to one and hence that demands that

$$\int_0^\infty e^{-\frac{t}{2}} \left[2\alpha \cosh(\alpha t) - \sinh(\alpha t)\right] \mathrm{d}t = 0, \tag{34}$$

which it does. Then we note that both γ and K are functions of k_{ij} and hence are not fully independent parameters. Examining the structure of K and γ, first we note that

$$K = \frac{k_{LC}}{k_{CE}} \gamma^2 \tag{35}$$

and that the maximum value of γ is when $k_{CL} = 0$ and thus as a function of k_{LC} and k_{CE}, the maximum value of γ is

$$\gamma = \frac{1}{1 + \frac{k_{LC}}{k_{CE}}} \quad \rightarrow \quad \gamma = \frac{1}{1 + \frac{K}{\gamma^2}} \tag{36}$$

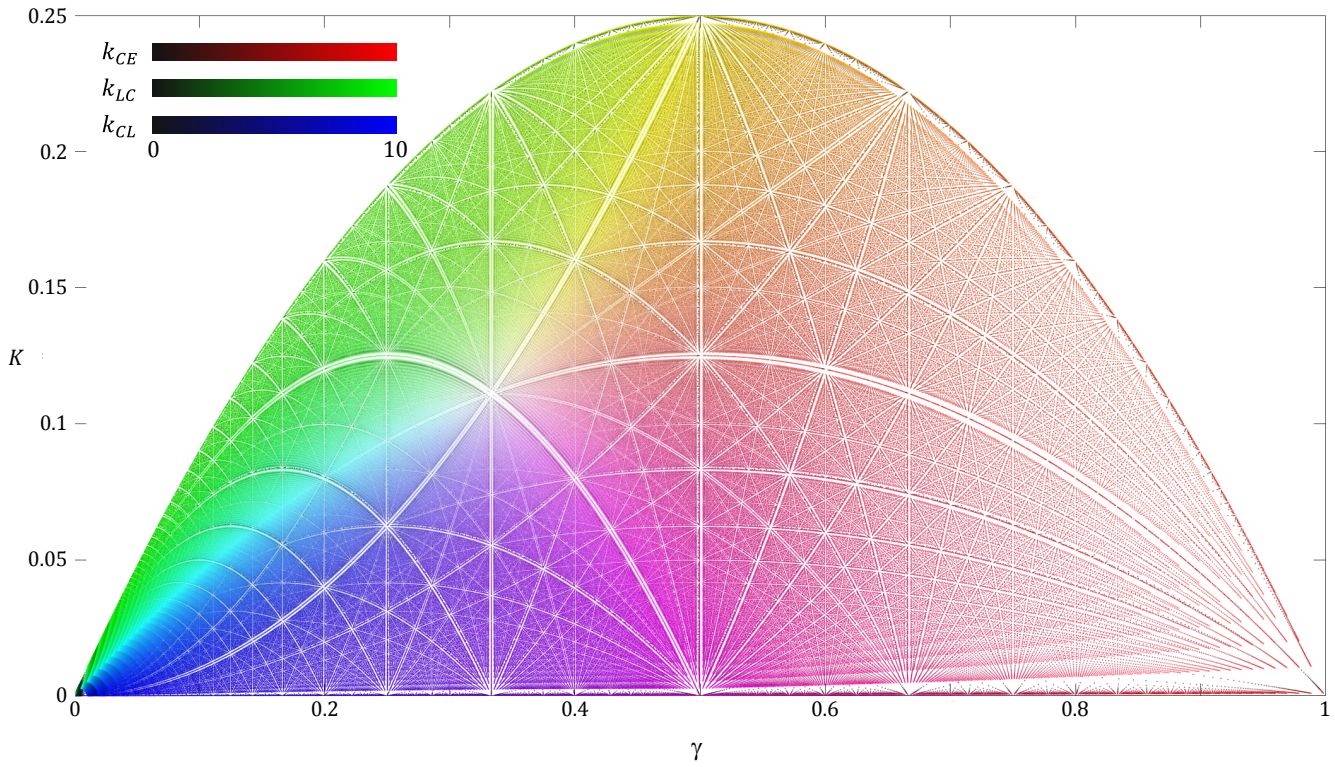

SI Figure 10: The two dimensionless rate parameters K and γ are not fully independent of each other because they are both functions of k_{ij} and $k_{ij} > 0$. As shown in this text, $K \leq \gamma(\gamma - 1)$, here shown by the bounding parabola, where the values within that region are fractally organized. We do not yet know the full mapping from this kinetic parameter space to the morphological space specified by R and Δx.

Thus the maximum value of K is bounded by

$$K \leq \gamma(1 - \gamma) \tag{37}$$

and the minimum is zero. Any arbitrary (arb) initial condition is a weighted sum of these two solutions for the extinction probability

$$p_{\text{arb}} = (1 - f)p_{01}(t) + fp_{10}(t) \tag{38}$$

with $0 < f < 1$ being the weighting. Then because p_{01} and p_{10} share terms this simplifies to

$$p_{\text{arb}}(t) = \frac{K}{\alpha} e^{-\frac{t}{2}} \sinh(\alpha t) + f\gamma \frac{e^{-\frac{t}{2}}}{2\alpha} \left[2\alpha \cosh(\alpha t) - \sinh(\alpha t)\right]. \tag{39}$$

While we know that K and γ obey $K \leq \gamma(1 - \gamma)$, f is an independent parameter.

Examining our simulations, the fit parameters to the output distributions have a wide range of K, given that $0 < K < 1/4$, suggesting that $\gamma \sim \frac{1}{2}$ for most simulations and hence that $k_{CE} \sim k_{CL} + k_{LC}$. Likewise, we found that fitting bounded $f \ll 1$. This parameter regime suggests that simulations tend to start off in the limit-cycle phase and migrate to the chaotic phase before going extinct. In fitting the extinction time distributions, we fit for both K and τ, ignoring γ because $f \ll 1$, and we allowed for a small time translation $t \to t - t_o$ to account for the 'grow-in' period from random initial conditions. Finally, we note that this transition state model is valid for the connection diagram shown in SI Fig. 9 when those state transitions have well-defined average rates (k_{ij}); the transition-state model is not specific to the PDEs of our ecological model.

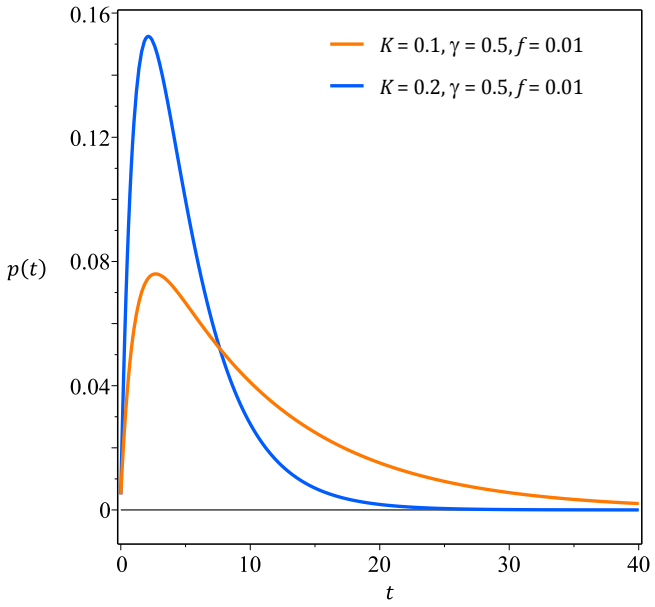

SI Figure 11: Examples of the extinction time distributions for values of K, γ, and f that are similar to what we see from our simulations.

5 Classification of Dynamic States

See SI Fig. 12.

6 Extinction Dynamics in Asymmetric Lattices

See SI Fig. 13.

7 Supplemental Movie Legends

Supplemental Movie 1: Symmetric two-species competition in structurally isotropic and anisotropic environments. Simulation parameters are $L/(1.29\lambda) = 100$, $P = 0.1$, $A_{\min} = 0.001$ with $R/(1.29\lambda) = 2$ and $\Delta x = 3.5R$ for the anisotropic case. The movie depicts system dynamics over 1200 doubling times; the anisotropic simulation is pinned after approximately 160 doubling times. Snapshots of these simulations were used to make Figure 1.

Supplemental Movie 2: Pinning and coexistence of species with asymmetric competitive fitness. Simulation parameters are $L/(1.29\lambda) = 100$, $P_{AB} = 0.112$, $P_{BA} = 0.088$, $A_{\min} = 0.001$, $R/(1.29\lambda) = 2$ and $\Delta x = 3R$. The movie depicts system dynamics over 85 doubling times.

Supplemental Movie 3: Large and widely spaces pillars do not significantly perturb intransitive communities. Simulation parameters are $L/(1.29\lambda) = 100$, $P = 0.1$, $A_{\min} = 0.01$, $R/(1.29\lambda) = 8$, $\Delta x = 5R$. The movie depicts system dynamics over 1,000 doubling times.

Supplemental Movie 4: Dense pillars induce wave destabilization and community collapse. Simulation parameters are $L/(1.29\lambda) = 100$, $P = 0.1$, $A_{\min} = 0.01$, $R/(1.29\lambda) = 10$, $\Delta x = 2.6R$. The movie depicts system dynamics over 1,000 doubling times.

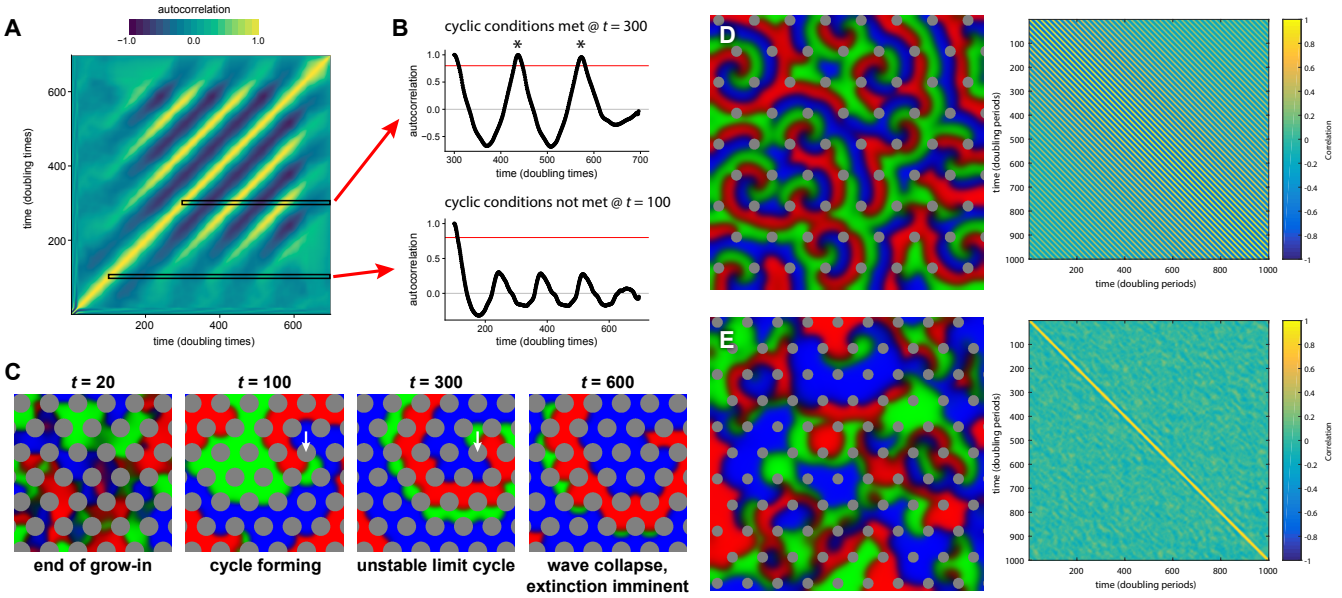

SI Figure 12: Classification of intransitive community dynamics. (A) For every simulation, the temporal autocorrelation was calculated using the vectorized pixel intensities of all species for every non-pillar pixel in the system. (B) The resulting autocorrelation matrix was then used to determine if the spatial distributions of species recapitulated themselves to a sufficiently high degree for at least two cycles; if so, the simulation was classified as cyclic at that time point. A threshold correlation of 0.8 was chosen (red line), as this was the level at which isotropic simulations were reliably classified as cyclic over $\sim$ 1000 doubling times (excluding grow-in and time points fewer than two cycles from the end of the simulation). The resulting time-dependent classifications were used to generate Figure 5A. The data for this figure was taken from a simulation with $L/(1.29\lambda) = 100$, $P = 0.1$, $A_{\min} = 0.01$, $R/(1.29\lambda) = 6$ and $\Delta x = 3R$. (C) Snapshots of this simulation corresponding to distinct dynamic regimes. After a short grow-in period, the simulation relaxed into a limit-cycle driven by a single wave center about one of the pillars (white arrow at $t = 100$ and 300). This wave center was unstable (note asymmetric species distributions about the pillar at $t = 100$ and 300 and wave widths at $t = 300$), persisting for several hundred doubling times until collapse of the wave center resulted in an extinction cascade at $t = 700$ (trivial autocorrelations of the victorious monoculture that persisted until the end of the simulation are not included in the analysis). (D) and (E) show snapshots and corresponding autocorrelation matrices for the stable limit-cycle from Fig. 3B and the persistent chaotic state from Fig. 3D, respectively, to demonstrate the clearly observable differences in their autocorrelation structure. In both simulations $L/(1.29\lambda) =$, $D = 15$, $P = 0.1$, $A_{\min} = 0$, $R = 15$, and in (D) $\Delta x = 6.5R$, while in (E) $\Delta x = 5R$.

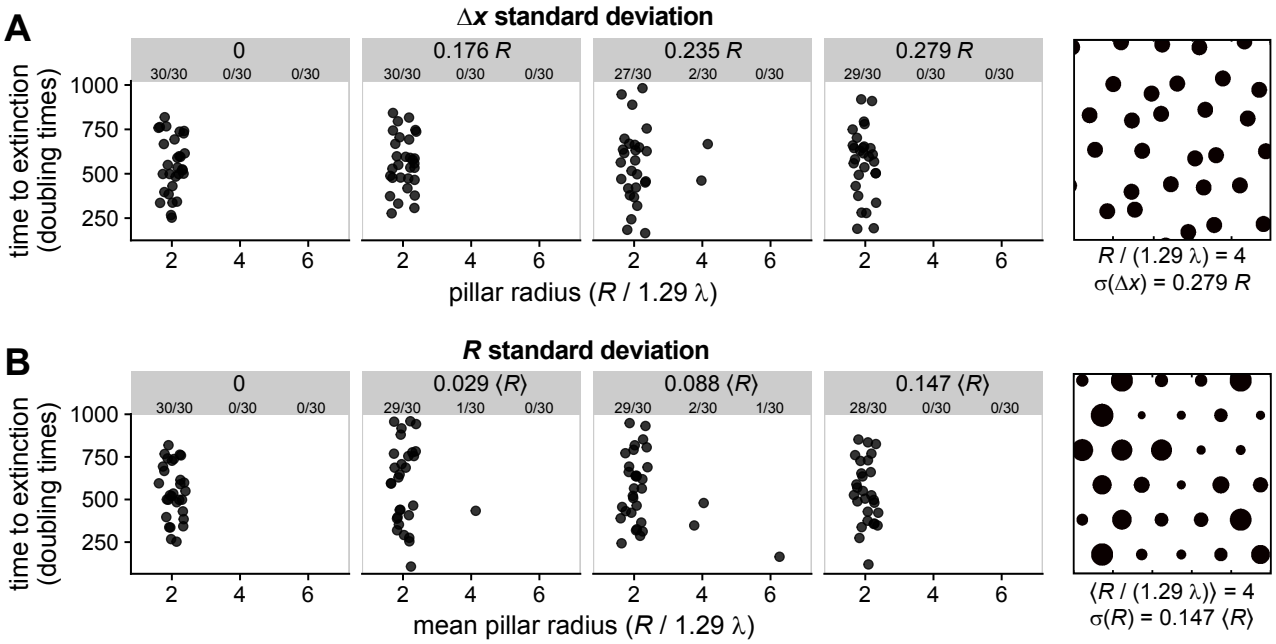

SI Figure 13: Randomized pillar arrays do not affect qualitative community outcomes. Pillar arrays were randomized by drawing either the pillar spacing Δx (A) or the pillar radius R (B) from a uniform distribution of varying width. In (A) pillar positions were randomized by jittering pillar positions, with the displacement direction chosen randomly and the displacement magnitude drawn from a uniform distribution with mean $5R$ and standard deviation as indicated in panel headings. In (B) the positions remained fixed to a triangular grid but the pillar radii varied, drawn from a uniform distribution with the indicated mean and variance. Example randomized arrays are shown on the right. For each standard deviation, three independent realizations of the jittered grid of pillars were generated and manually validated to ensure pillars were not overlapping or spaced too closely to accurately simulate diffusion. Ten random initial condition replicates were performed for each of the three grids, giving 30 total simulations for each standard deviation in Δx or R. Fractions within subheadings of each panel indicate the observed frequency of extinction for each condition. In all cases, extinction frequency did not show a significant dependence on the standard deviation of Δx nor R, whereas extinction frequency showed a strong dependence on mean lattice parameters, consistent with observations in the main text. Plotted points are randomly displaced along the x-axis to reduce overlap. Simulation parameters are $L/(1.29\lambda) = 100$ and $P = 0.1$, with indicated pillar radius R and spacing $\Delta x = 5R$ before addition of random variation as indicated.

Supplemental Movie 5: Pillars may serve as unstable wave centers. Simulation parameters are $L/(1.29\lambda) = 100$, $P = 0.1$, $A_{\min} = 0.01$, $R/(1.29\lambda) = 6$, $\Delta x = 3.4R$. The movie depicts system dynamics over 1,000 doubling times.

Supplemental Movie 6: Small dense pillars can cage wave centers and prolong community coexistence under chaotic dynamics. Simulation parameters are $L/(1.29\lambda) = 100$, $P = 0.1$, $A_{\min} = 0.01$, $R/(1.29\lambda) = 2$, $\Delta x = 2.4R$. The movie depicts system dynamics over 1,000 doubling times.

Supplemental Movies 7 - 10: Spatiotemporal evolution of species concentration fields from Figure 3. Simulation parameters are $L/(1.29\lambda) = 150$, $P = 0.1$, $A_{\min} = 0$, $R/(1.29\lambda) = 3$, Δx as indicated in Figure 3. The movies are time stamped in doubling times.

References

[1] Holger Kantz, 'A robust method to estimate the maximal Lyapunov exponent of a time series', *Physics Letters A* **185**, p. 77-87, 1994.